Journal of Materials Science: Metallurgy

RESEARCH Open Access

Effect of thermomechanical processing on mechanical properties and the microstructure of ternary Al-Ce-Mg alloy

Gaurav Singh[1], Humphrey Wara Odhiambo[2], Mohamad Hasan Bin Tasneem[1], Gaoyuan Ouyang[2,3*], Monica A. Soare[4], Min-chul Kang[3], Lin Zhou[3], Jun Cui[2,3], Ralph E. Napolitano[2] and Catalin R. Picu[1*]

Abstract

Al-Ce alloys are known to retain a large fraction of their room temperature properties at elevated temperatures and after exposure to temperature for extended periods. Here we work with the ternary close-to-eutectic alloy Al-10Ce-4Mg and explore the effect of extrusion on its microstructure and mechanical properties. Extrusion produces a highly refined microstructure with texture exhibiting a twofold increase in strength (tensile strength of 390 MPa at room temperature) and fourfold increase in failure strain relative to the as cast state. After exposure to 300 °C for 100 h the alloy retains 82% and 88% of the room temperature strength in the as-cast and extruded states, respectively. The ratio of the strength at 300 °C to the strength at room temperature is 0.4, below the corresponding ratio for the Al-10Ce binary alloy (ratio 0.7) but higher than that of AA2618 (ratio 0.1). The extruded Al-10Ce-4Mg has fracture toughness of 23 kJ/m^2, which is retained in proportion of 97.6% after exposure to 300 °C for 100 h. The material exhibits negative strain rate sensitivity at room temperature and in the range of strain rates $10^{-5}\ s^{-1}$ to $10^{-2}\ s^{-1}$. We show that the high room temperature strength is due to $Al_{11}Ce_3$ dispersoids and Mg-rich precipitates. The Mg-rich precipitates dissolve in the temperature range 200 °C to 250 °C while the $Al_{11}Ce_3$ dispersoids remain stable and provide strengthening at 300 °C. Mg-rich precipitates reform upon cooling, which ensures property retention upon thermal cycling. The high toughness, strength and property retention upon exposure to elevated temperatures make this alloy an excellent candidate for applications requiring lightweight temperature resistant materials.

Keywords Al-Ce-Mg alloy, Mechanical Properties, Microstructure, Fracture toughness, Extrusion

*Correspondence:
Gaoyuan Ouyang
gaoyuan@iastate.edu
Catalin R. Picu
picuc@rpi.edu
[1]Department of Mechanical, Aerospace, and Nuclear Engineering, Rensselaer Polytechnic Institute, Troy, NY 12180, USA
[2]Department of Materials Science & Engineering, Iowa State University, Ames, IA 50011, USA
[3]Division of Materials Sciences and Engineering, Ames National Laboratory, Ames, IA 50011, USA
[4]GE Aerospace Research, Niskayuna, NY 12309, USA

Introduction

A need exists for light materials with enhanced thermal stability to be used in supersonic aircraft design. The use of Al alloys would provide higher fuel savings, lower CO_2 emissions, and overall increased energy efficiency. However, the use of current Al alloys from the AA2XXX and AA7XXX class, which are precipitate hardened, is impossible as their properties degrade above ~ 200 ? due to the dissolution and/or coarsening of precipitates(Gao et al. 2019)(Mondol et al. 2017). In contrast, the Al-Ce intermetallics are highly stable and resist coarsening up to at least 350 °C (Guo et al. 2022, Shen et al. 2023, Nam et al. 2023, Singh et al. 2024). This drives the emergence of a new generation of castable Al-Ce alloys with significantly improved high-temperature strength (Shen et al. 2023, Stojanovic et al. 2018, Sims et al. 2016, El-Hadad et al. 2023, Weiss and Cerium 2019, Huda and Edi 2013).

Ce is a relatively abundant rare earth element (REE) which may be obtained as a byproduct of the extraction and purification of more valuable REEs, including Li, Pr, Nd, Dy, and Tb (Sims et al. 2022). Cerium lacks high-volume applications at present time (Weiss and Cerium 2019, Czerwinski 2019). When added to Al as an alloying element, Ce forms the $Al_{11}Ce_3$ intermetallic, with an eutectic point at 10% Ce (Sims et al. 2017) (all percentages in wt%). Microstructures with off-eutectic compositions contain a dominant Al (fcc) phase for hypoeutectic, and script-like (or plate-shaped) $Al_{11}Ce_3$ intermetallics in the case of hypereutectic alloys (Perrin et al. 2023, Okamoto 2011, Cao et al. 2017, Dai et al. 2023, Sun et al. 2019, Kozakevich et al. 2023, Ye et al. 2023, Rogachev and Naumova 2021). The non-uniform distribution of the intermetallics in the as-cast state leads to sub-optimal strengthening. Nevertheless, Al-Ce alloys in the near-eutectic range (5–15% Ce) exhibit excellent castability and resistance to hot tearing and cracking (Plotkowski et al. 2020).

Ce has low diffusivity and solubility in the Al (fcc) phase (Okamoto 2011) which implies slow dissolution and Ostwald ripening of precipitates at elevated temperatures and hence superior temperature stability of these alloys (Singh et al. 2024, El-Hadad et al. 2023). To benefit from this exceptional behavior, it would be necessary to ensure high strength and ductility/toughness at room temperature. To this end, a uniform dispersion of fine intermetallics is desirable(Rogachev et al. 2021). This has been achieved by additive manufacturing (Nam et al. 2023, Sisco et al. 2021) and by thermo-mechanical processing of cast alloys (Singh et al. 2024, D'Souza et al. 2019, Zhang et al. 2021). Despite significant enhancement of the room temperature yield stress and strength of binary Al-Ce alloys processed by these methods, the performance remains below that of high strength commercial Al alloys. To address this problem, strengthening of the Al matrix has been pursued by alloying to promote either solid solution hardening or precipitation strengthening associated with other alloying elements.

Several studies evaluated the effect of Mg on the microstructural and mechanical properties of cast and additive-manufactured Al-Ce alloy (Nam et al. 2023, Sisco et al. 2021, Czerwinski et al. 2022, Gröbner et al. 2002, Lv et al. 2022, Hu et al. 2021). Hu et al. studied the effect of solid solution strengthening in high-pressure die-casting Al–Ce–Mg alloys. They suggest that the work hardening of Al–8Ce-yMg increases as the Mg content, 'y', increases from 0 wt% to 0.75 wt% (Hu et al. 2021). Nam et al. studied ternary alloys (Al-8Ce-10Mg, Al-16Ce-1Mg) produced by additive manufacturing over a wide composition range (Nam et al. 2023). Weiss et al. studied the addition of 10% Mg in an Al-8Ce alloy, indicating an increase of the yield stress from ~ 50 MPa to ~ 162 MPa (Weiss and Cerium 2019). Forging, rolling, extrusion, high-pressure torsion and equal-channel angular pressing (ECAP), have been used to produce microstructural refinement in metals and alloys and some of these procedures have been also applied to Al-Ce alloys (Singh et al. 2024, Wang et al. 2022).

Conventional processing methods such as extrusion and rolling need to be explored in this context to facilitate industrial adoption of these materials. Extrusion was suggested as being effective in refining the microstructure of Al-Ce binary alloys (Singh et al. 2024). Extrusion of binary Al-Ce was also reported in(Sims et al. 2017) as a method to increase the strength over the cast state. Wang et al.(Wang et al. 2020) report processing Al-Ce-X (X = Sc, Y, Zr) by extrusion, but only for low (0.2%) Ce concentrations. Milligan et al.(Milligan et al. 2024) process Al-8Ce-4Mg using a non-conventional method that combines extrusion and torsion to enhance the total plastic strain and report significant enhancement of strength due to microstructural refinement.

In this work we consider the Al-10Ce-4Mg alloy. Al-10Ce is the eutectic composition, which was demonstrated previously to have optimal room temperature mechanical properties among the binary alloys (Singh et al. 2024, Odhiambo et al. 2025). We introduce microstructural refinement by conventional extrusion to render the study relevant for industrial applications. We provide full characterization of mechanical properties at room and elevated temperatures, including toughness and hardness, in conjunction with microstructural characterization. Microstructural characterization is performed using scanning electron microscopy (SEM), X-ray diffraction (XRD), electron backscatter diffraction (EBSD), differential scanning calorimetry (DSC) and high resolution transmission electron microscopy (HRTEM). Uniaxial tensile testing is performed at ambient and elevated temperatures, as well as in ambient conditions after exposure to elevated temperatures. Fracture toughness testing is performed in ambient conditions, before and after exposure to elevated temperatures. The degree of microstructural refinement retention and thermal stability are evaluated for both cast and extruded states. This article provides the first report of fracture toughness and strain rate sensitivity measurements of Al-Ce-Mg alloys, and a detailed characterization of the microstructure and thermo-mechanical properties of close-to-eutectic compositions of the Al-Ce-Mg system upon processing by pure extrusion.

Experimental

Materials and processing

Al-10Ce-4Mg alloys were prepared by mixing Al with Al-Ce and Al-Mg master alloys (Al-20Ce and Al-50Mg). The materials used are high purity raw materials acquired from Ames Lab Materials Preparation Center. The two homogenous and high purity master alloys were acquired from AGI Alloys Inc. Pure Al was heated in a graphite crucible to 850 ? and held for at least 30 min before Al-Ce and Al-Mg master alloys were added into the melt. The molten alloy was then vigorously mixed for at least 10 min before it was poured into a 25.4 mm diameter graphite mold preheated to 400 °C. The actual composition of the sample was determined by Inductively Coupled Plasma – Optical Emission Spectroscopy (ICP-OES) with a resolution of 0.01 ppm. The results indicate 85.162% Al, 10.096% Ce, 4.676% Mg, 0.029% Fe and 0.037% Si (all wt%).

The specific addition of 4 wt% Mg was chosen here for utility in the investigation of thermomechanical processing effects because it provides an opportunity to perform deformation above and below the relevant intermetallic solvus boundaries, within the range of ~290 °C to 310 °C. For the specific experiments described here, the selected deformation and annealing temperatures are at or just below the τ-$Al_{13}CeMg_6$ solvus and above the metastable β-AlMg solvus. This affords the opportunity to utilize the high dislocation density generated during deformation to stimulate nucleation of fine intermetallics either at this temperature, or upon subsequent cooling below the β-AlMg solvus. These determinations are based on CALPHAD modeling of Al-Ce-Mg phase equilibria using the assessed parameters reported in (Moore et al. 2020).

The cast rods were hot extruded to a final diameter of 9.5 mm using an Innovare LMS extrusion press. This was done by heating to 300 ?, holding isothermally for 30 min, extruding through a steel die at an average rate of (96.2 MPa/min) with a maximum pressure of 560 MPa, and forced-air cooling to room temperature. The total reduction during extrusion was 86%, which corresponds to a plastic strain of 1.97.

Table 1 Materials and conditions considered in the present study

Naming convention	Description
AC	As cast
CE	Cast and extruded
AC-10	As cast + 300 °C for 10 h
AC-100	As cast + 300 °C for 100 h
CE-10	Cast and extruded + 300 °C for 10 h
CE-100	Cast and extruded + 300 °C for 100 h

Properties were measured in the as-cast (AC) and cast and extruded (CE) conditions, and also in the corresponding heat-treated conditions (AC-10, AC-100, CE-10, CE-100), where 10 and 100 indicate the number of hours of exposure to 300 °C. Table 1 summarizes the test alloys and conditions considered in this study.

Tensile and fracture toughness experiments

Tensile specimens of 52 mm gauge length for all cast, extruded, and heat-treated conditions were CNC machined per the ASTM E8 standard (E8/E8M 2013). An Instron 5969 machine with a 50kN load cell was used for testing under quasi-static conditions ($\dot{\epsilon} = 3 \times 10^{-4}\, s^{-1}$). The extensometer used in all tensile tests at room temperature was an Epsilon Technology Corp. Model 3542 clip-on axial extensometer with a 10 mm gauge length. Tests were performed at room temperature (25 ?) and at elevated temperatures of 150 ?, 200 ?, 250 ? , 300 ? and 350 ?. For testing at temperature, samples were heated at 5 $?/s$ followed by a 300 s hold after the target temperature was reached and before the beginning of the test. Samples were kept at the target temperature for the duration of the test. Deformation at temperatures above room temperature was measured by the machine (not with an extensometer). Tensile testing was also performed with the same Instron 5969 machine equipped with a 50 kN load cell at various strain rates ($\dot{\epsilon} = 3 \times 10^{-2},\ 3 \times 10^{-3}, 3 \times 10^{-4}\ and\ 3 \times 10^{-5}\, s^{-1}$).

A microhardness tester (Qness 60 M QATM) with a load of 500 g and 15 s dwell time was used for hardness measurements, as per the ASTM E92 standard (E384-17 2016). Ten measurements were made for each sample condition, and the average values are reported.

The elastic-plastic fracture toughness (J_{Ic}) was measured in a single-edge bend test configuration (ASTM E1820 standard 2009) using the Instron frame also employed for uniaxial testing (ASTM). Sample dimensions were 12 × 6 × 60 mm and the loading span was 50 mm. Fatigue loading with amplitudes of 0.10 to 0.20 kN was performed before the toughness test, such to generate a sharp pre-crack extending for 1.2 mm from the machined notch. The pre-crack and the notch were oriented normal to the extrusion direction. The crack length to sample width ratio was 0.5. The toughness test (static bending) was performed at room temperature with a constant strain rate of $5 \times 10^{-3}\, s^{-1}$.

Microstructure characterization

To prepare samples for XRD and metallographic (SEM/EBSD) analysis, grinding was done with abrasive papers (320, 800, and 1200 grit), after which polishing was performed with cloths containing an abrasive suspension of alumina and colloidal silica, 5 µm to 0.05 µm. XRD was performed with a Panalytical XRD instrument with Cu-K_α radiation, between 20° to 90°, and at a scan rate of 1° per minute. Imaging (for metallography and fractography) was done using a FEI SEM. For this purpose, surfaces were etched with Kellar's reagent for 10 s after polishing. The inspection of fracture surfaces was performed without polishing and etching.

An Oxford SEM microscope was used for EBSD. The EBSD specimens' preparation required additional polished steps using diamond and colloidal silica to minimize surface deformation. The analysis of EBSD images was performed using MTEX software. The mapping is based on the fcc Al and orthorhombic $Al_{11}Ce_3$.

Transmission electron microscope (TEM) samples were prepared with a focused ion beam instrument with a gas injection system (Helios, Thermo Fisher Scientific Ltd.) and investigated with an aberration-corrected TEM (Titan Cube, Thermo Fisher Scientific Ltd.) at 200 kV acceleration voltage. STEM-EDS was taken at 200 kV acceleration voltage with 40 pA current.

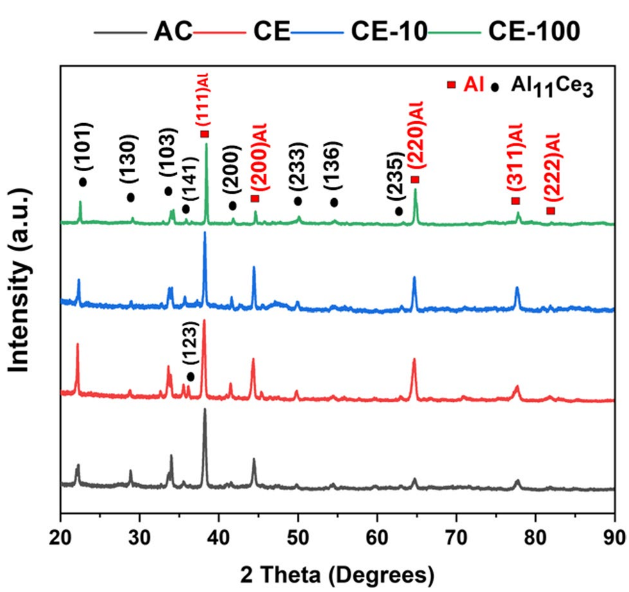

Fig. 1 XRD of Al-10Ce-4Mg for as cast (AC), extruded (CE), extruded and heat treated at 300 °C for 10 h (CE-10), and 100 h (CE-100)

Results

Phase analysis

Figure 1 shows the normalized XRD spectra for as-cast, as-extruded, and extruded and heat treated Al-10Ce-4Mg. The spectra indicate the presence of the α-Al FCC phase and $Al_{11}Ce_3$ intermetallic phase. Prominent α-Al peaks are (111), (220), (200) and (311) in all material states considered. The intensity of the Al (200) and Al (220) peaks (relative to the Al (111) peak) increases after extrusion (CE) compared with the as cast state (AC), indicating the development of texture. The (101), (141) and (200) peaks of the $Al_{11}Ce_3$ intermetallic phase also increase. Annealing for 100 h leads to a decrease of the Al (200) and Al (311) peaks which suggests a more random texture in CE-100 compared to CE and CE-10. No evidence of phase transformations taking place during extrusion and heat treatment is obtained. Similar observations have been made in the binary Al-10Ce alloy (Singh et al. 2024). No direct evidence of Al-Mg phases is visible in the diffractogram.

Microstructural evolution during extrusion and subsequent annealing

Scanning electron microscopy

The microstructure of Al-10Ce-4Mg in AC, CE, CE-100 states is shown in Fig. 2(a-c). Two phases are visible in these micrographs: the α-Al (fcc) matrix and the $Al_{11}Ce_3$ intermetallic. No phase containing Mg is visible at this magnification (see Section High temperature mechanical properties for further discussion of Mg-containing phases). The as cast micrograph, Fig. 2a, shows the eutectic microstructure commonly observed in the Al-10Ce binary alloy (Singh et al. 2024). Extrusion leads to a fine distribution of $Al_{11}Ce_3$ intermetallics in the Al matrix, as shown in Fig. 2b, which remain plate-like upon extrusion, but are shorter and become preferentially aligned in the extrusion direction. Phase fractions and phase compositions are statistically identical among the three states shown, indicating thermodynamic stability. In addition, the precipitate sizes are 3.57 ± 1.56 µm, 1.91 ± 1.12 µm and 2.51 ± 1.02 µm for AC, CE, and CE-100 states, respectively, showing refinement due to deformation and the resistance to coarsening of the refined structure. The SEM-EDX analysis of CE-100 (Al-10Ce-4Mg) is shown in the Supplementary information (S1), Fig. S1(a-d). This analysis indicates that, with the resolution of this probe (5 nm), Mg is present in solid solution or potentially small clusters in the α-Al phase; this conclusion is revisited in Section High temperature mechanical properties.

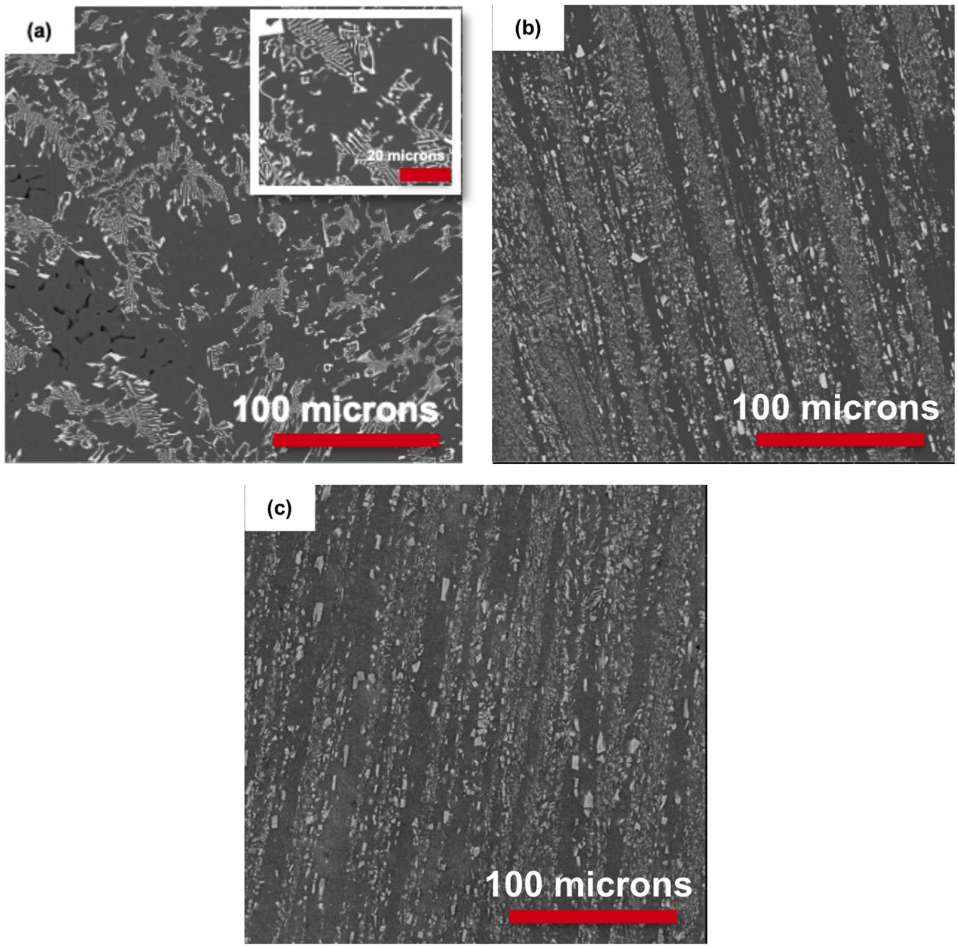

Fig. 2 The microstructure of Al-10Ce-4Mg (**a**) AC, (**b**) CE, (**c**) CE-100 samples, (black = Al, gray = $Al_{11}Ce_3$). The zoom-in in (**a**) shows the script-like phase which is characteristic for the eutectic Al-Ce phase

Electron backscattered diffraction

Electron backscattered diffraction (EBSD) provides the grain size, grain misorientation, phase fraction, micro strain, and texture information in the as cast, extruded and heat-treated alloys. EBSD analysis (100 nm resolution) includes the computation of pole figure (PF), inverse pole figure (IPF), and kernel averaged misorientation (KAM). Figure 3a-c shows EBSD data for as cast Al-10Ce-4Mg. The IPF map in Fig. 3a shows that the microstructure contains primary Al-Mg fcc solid solution phase and $Al_{11}Ce_3$ precipitates. The grain size was measured as 23.56 ± 0.76 μm. The script-like structure of the primary phase, Fig. 2a, observed here is similar to that seen in the binary Al-10Ce alloy (Singh et al. 2024). The high fraction of primary phase in both cases suggests that the eutectic coupled zone is skewed to higher Ce compositions, as common for faceted-non-faceted eutectics and previously shown experimentally for binary Al-Ce (Jones 2005). The phase map in Fig. 3b shows the spatial distribution of fcc and $Al_{11}Ce_3$ phases, with a measured area-based intermetallic phase fraction of 0.13. The average precipitates size is 3.57 ± 1.56 μm, but larger cuboidal precipitates are also present. The average misorientation across grain boundaries is 20.34°. The KAM map of the cast samples is shown in Fig. 3c with an average KAM value of 0.59, which indicates the distribution of microstrain in the as cast state. This information is used to calculate the density of geometrically necessary dislocations later in this section.

Figures 4a-c shows the EBSD IPF maps of Al-10Ce-4Mg in the CE, CE-10, and CE-100 conditions. All samples show heterogeneous microstructures, with different grain sizes in different regions: strip-like regions oriented in the extrusion direction, with larger grains also elongated in the extrusion direction, are separated by finer grains. A similar observation has been made for binary Al-Ce in our previous work (Singh et al. 2024). The average grain size for (111) oriented grains is 5.6 ± 2.6 μm, 5.8 ± 2.6 μm, and 9.2 ± 7.3 μm for CE, CE-10, and CE-100 conditions, respectively. The average grain size for (101) oriented grains is 7.9 ± 4.3 μm, 9.8 ± 6.9 μm, and 8.4 ± 5.4 μm for CE, CE-10, and CE-100 conditions,

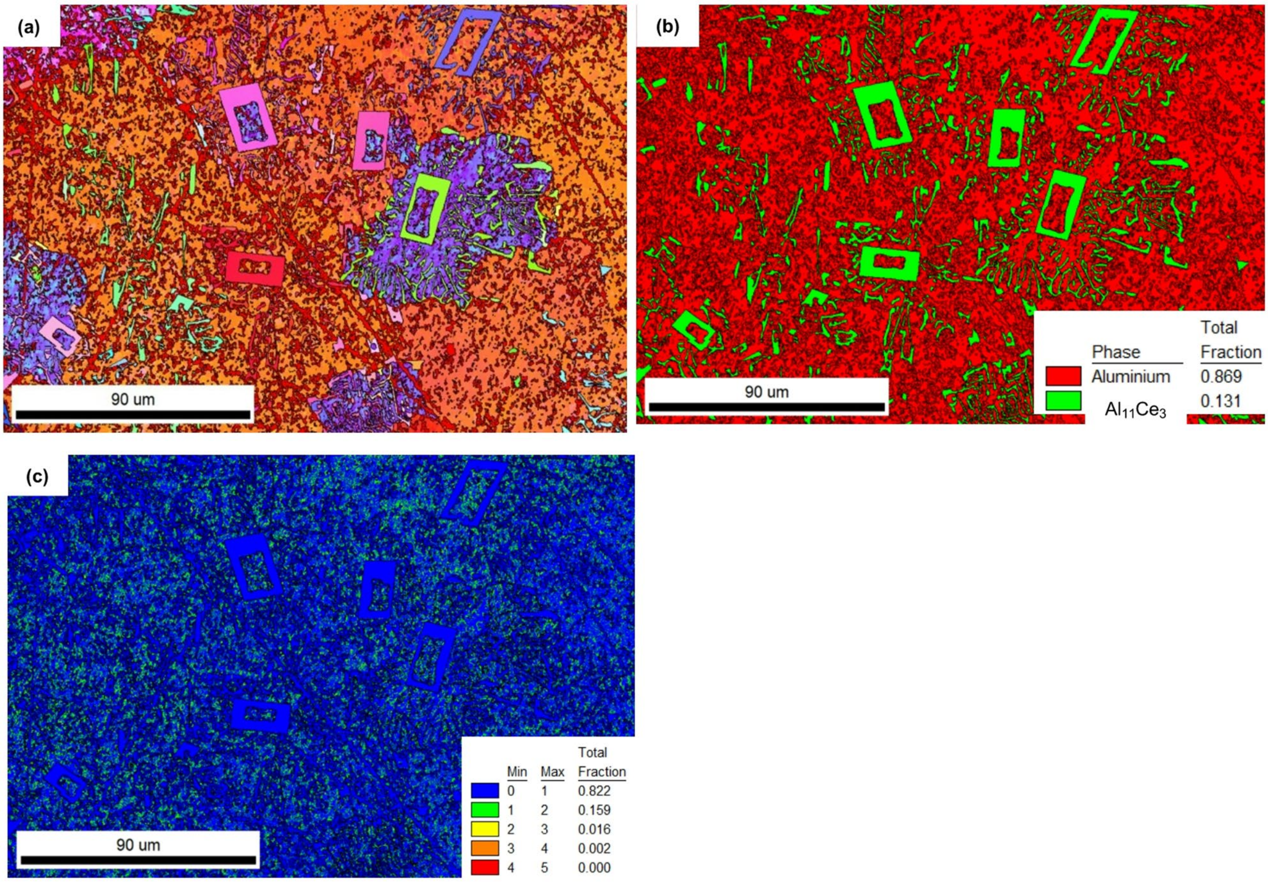

Fig. 3 EBSD of as-cast Al-10Ce-4Mg (**a**) IPF map, (**b**) Phase map (**c**) KAM map. Large, rectangular, and fine, script-like, $Al_{11}Ce_3$ intermetallics are visible in (**b**)

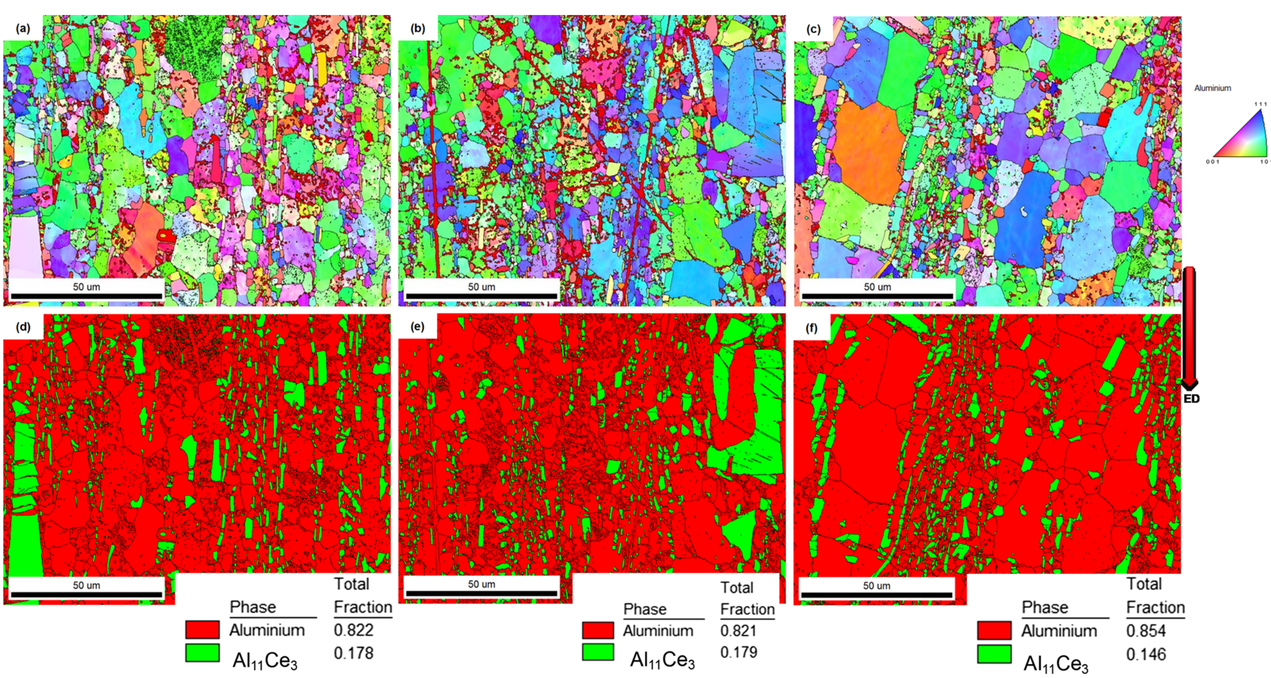

Fig. 4 IPF maps of Al-10Ce-4Mg in the (**a**) CE, (**b**) CE-10, (**c**) CE-100 states. The phase maps corresponding to panels (**a**), (**b**) and (**c**) are shown in (**d**), (**e**) and (**f**), respectively

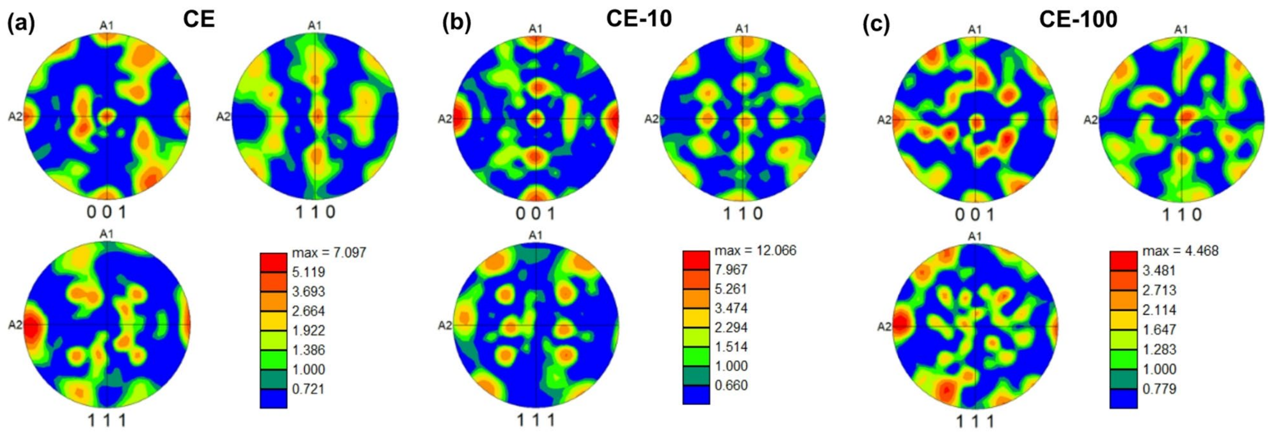

Fig. 5 Pole figure of (**a**) CE, (**b**) CE-10, (**c**) CE-100 for Al-10Ce-4Mg, A1 is the extrusion direction and A2 is transverse direction

respectively. Considering the large relative uncertainty in these measurements, the difference between the two orientations is not statistically significant. Considering now the full population of grain orientations, we compare the average grain size for the three material conditions, yielding values of 7.24 $\pm$ 5.88 µm, 7.08 $\pm$ 6.09 µm, and 10.22 $\pm$ 8.11 µm, for CE, CE-10, and CE-100, respectively, suggesting that high temperature exposure does not modify the grain size to any statistically significant degree. The grain size distribution is shown in S1, Fig. S2a.

The average dispersoid size is 1.91 $\pm$ 1.12, 2.22 $\pm$ 1.72, and 2.51 $\pm$ 1.02 µm for CE, CE-10, and CE-100, respectively. Consistent with the grain size measurements, this modest and statistically insignificant variation even after 100 h of annealing suggests good microstructural stability at 300 °C.

The average misorientation distribution is 26.57°, 29.06°, 29.82° for CE, CE-10, and CE-100, respectively. The distributions of misorientation are shown in Fig. S2b for the three states. Annealing leads to a slight shift of the misorientation distribution to higher angles. The fraction of high-angle grain boundaries (defined as boundaries with misorientation above 15°) is 0.60, 0.63, and 0.65 for CE, CE-10, and CE-100 sample conditions, respectively. The EBSD phase maps for the three states are shown in Fig. 4d-f. The $Al_{11}Ce_3$ phase volume fraction inferred from these images is 17.8% in the extruded state and 17.9% and 14.6% after annealing at 300 ? for 10 h and 100 h, respectively.

Figures 5a-c show the pole figure map in (001), (110), and (111) projections for CE, CE-10, and CE-100 conditions. Annealing for 10 h increases the intensity of the brass texture ({110}<112>)of CE sample, but the texture becomes somewhat less well defined upon annealing for 100 h. This feature is consistent with the XRD measurements (Fig. 1), where the intensity of the Al (200) and Al (220) peaks are observed to increase upon extrusion and then to decrease upon annealing for 100 h. This suggests a more random texture in CE-100 compared to CE and CE-10, which is further supported by the pole figure map, Fig. 5. Table 2 shows the maximum intensity of the pole figure and supports the described texture evolution (enhancement and weakening after 10 h and 100 h annealing, respectively). The influence of these texture variations on mechanical properties is discussed in Section Mechanical properties.

EBSD also provides the kernel average misorientation (KAM) values of the CE, CE-10, and CE-100 samples. This information is used to evaluate the dislocation density. The KAM map of CE, CE-10, and CE-100 are shown in Fig. 6a-c. The average KAM value of AC, CE, CE-10, and CE-100 are 0.59°, 0.59°, 0.62°, and 0.55°, respectively. The geometrically necessarily dislocations density, ρ_{GND}, is calculated based on the average KAM value using the strain gradient approach (Basu et al. 2018):

$$\rho_{GND} = \frac{2\theta}{n\lambda\,|b_D|}. \tag{1}$$

Here θ is the experimental KAM value, λ = 1 µm is the step size, n is the number of nearest neighbors

Table 2 Mean grain size, maximum texture intensity, and dislocation density (obtained from EBSD, ρ_{GND}) for AC, CE, CE-10, and CE-100 states of the Al-10Ce-4Mg alloy

	Mean grain size (µm)	Maximum Texture Intensity (m.r.d.)	Main texture component	EBSD (m^{-2})
AC	23.56	-	-	6.92*10^^{13}
CE	7.24	7.10	brass texture ({110}<112>)	$1.4{*}10^{14}$
CE-10	7.08	12.07	brass texture ({110}<112>)	$1.44{*}10^{14}$
CE-100	10.22	4.47	brass texture ({110}<112>)	$1.34{*}10^{14}$

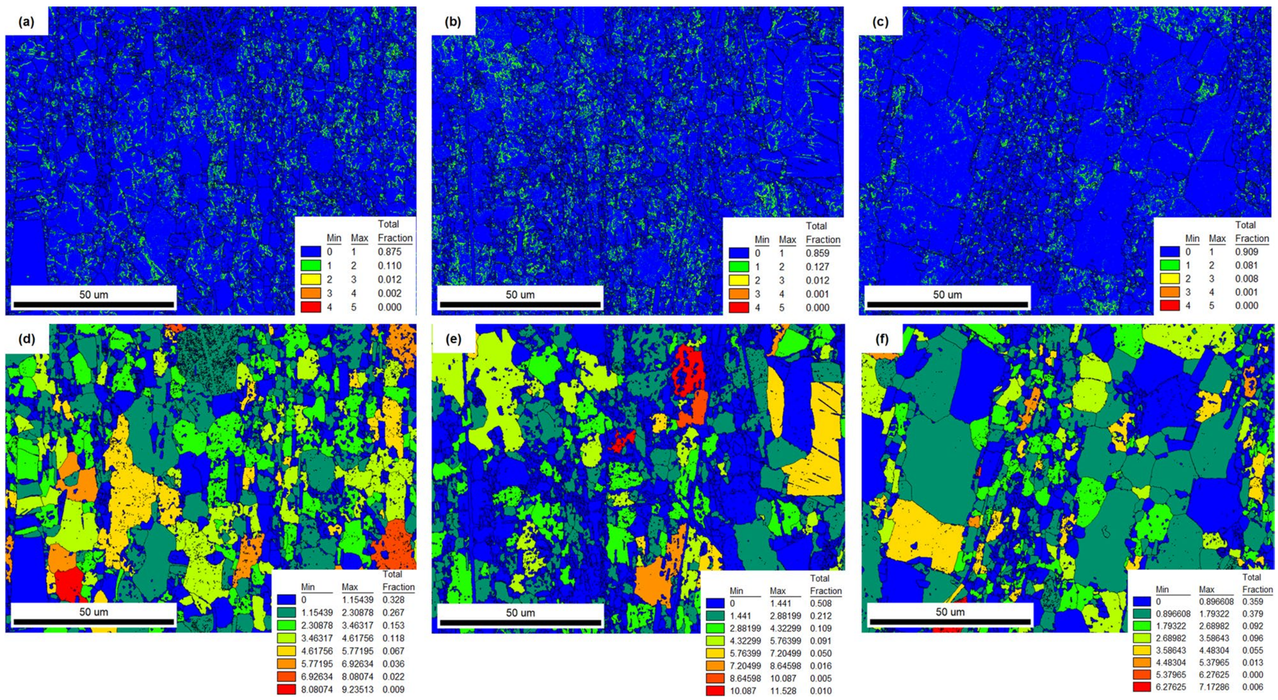

Fig. 6 KAM maps of Al-10Ce-4Mg in the (**a**) CE, (**b**) CE-10, (**c**) CE-100 states. The GOS maps corresponding to panels (**a**), (**b**) and (**c**) are shown in (**d**), (**e**) and (**f**), respectively

averaged in the KAM calculations (here it is 5), and b_D is the Burgers vector of the active slip system (b_D = 0.286 nm). The resulting dislocation density values are reported in Table 2. The dislocation density increases upon extrusion, as expected, it is essentially unchanged upon annealing for 10 h and decreases slightly upon annealing for 100 h. The GNDs depend on the microstructural characteristics, such as grain size, texture, and phase (Kamaya 2012, Sun et al. 2021). The grain size increase and texture intensity decrease lead to a slight reduction in dislocation density for annealed samples (100 h). The lack of a more drastic reduction of the dislocation density upon annealing indicates that the stable intermetallic distribution is effective at pinning dislocations.

The grain orientation spread (GOS) map is helpful in distinguishing strain-free (recrystallized; GOS ≤ 2°) and deformed grains (GOS > 2°). The GOS maps for the three states are shown in Fig. 6d-f. Recrystallization may be inferred from the GOS values, with recrystallization fractions for CE, CE-10, and CE-100 being estimated as 0.59, 0.62, and 0.73, respectively. It suggests that CE-100 contains more recrystallized grains, which is consistent with the observation of a more random texture (lowest texture intensity, as shown in Fig. 5c) upon annealing for longer times and a slightly lower dislocation density.

These results indicate that extrusion produces microstructural refinement (both smaller grains and smaller intermetallics), an increase of the dislocation density and the emergence of crystallographic texture. Annealing for 100 h does not substantially affect the mean grain and dispersoid size but decreases slightly the dislocation density and the texture intensity. No microstructural changes are observed upon annealing for 10 h. This suggests that the annealing time should have some influence on the mechanical properties, which is discussed further in Section Mechanical properties.

NNM O[OIP NBBPPKOBNJH,N .Mechanical properties

Mechanical properties of as cast and extruded Al-10Ce-4Mg

The room temperature engineering stress-strain curves of Al-10Ce-4Mg alloy in the AC, AC-10, AC-100 and CE, CE-10, and CE-100 conditions are shown in Fig. 7a. All AC samples (including after annealing) have rather poor mechanical properties, with strength below 150 MPa. The extruded (CE) samples have significantly improved properties: the yield stress and tensile strength increase by 2 and 3 times, respectively, while the elongation at failure increases ~ 5 times, from 3.8% to 17.2%. Young's modulus results E = 75 GPa. The simultaneous improvement in strength and ductility is attributed to microstructural refinement, increased uniformity of the distribution of the $Al_{11}Ce_3$ intermetallics and the texture caused by extrusion. The mechanisms leading to the increase of strength are discussed further in Section Considerations related to the strengthening mechanisms. We associate the increase of ductility to the development of texture during extrusion. Structural refinement includes both the

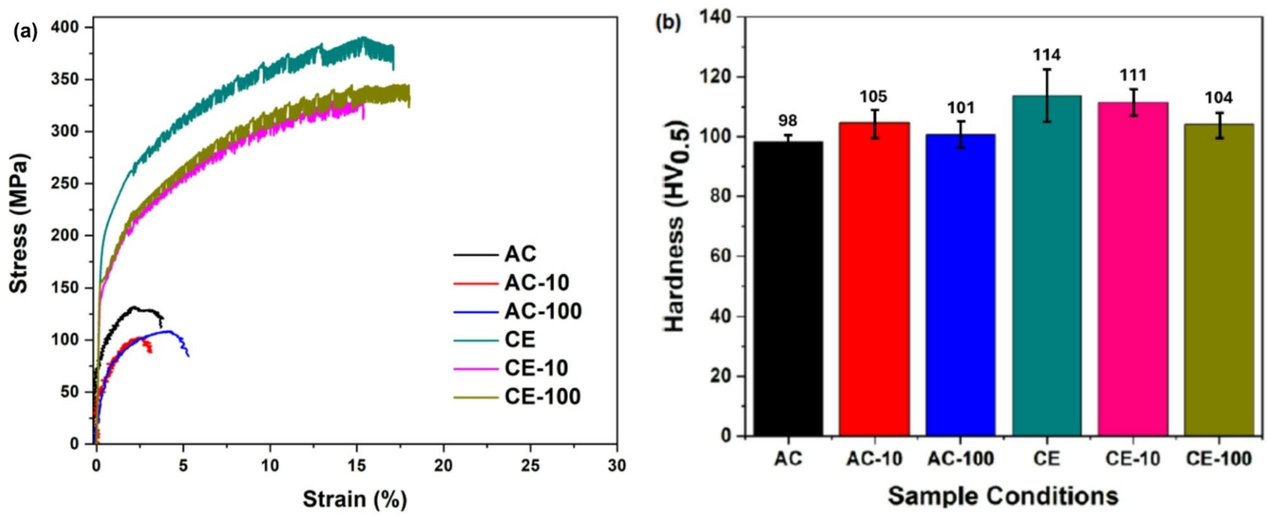

Fig. 7 (**a**) Room temperature engineering stress-strain curves of extruded and cast Al-10Ce-4Mg samples tested with a strain rate of $\dot{\epsilon} = 3 \times 10^{-4}\, s^{-1}$, and (**b**) hardness measured at room temperature for the same set of samples

size and shape of the dispersoids, with the shape changing from thin interconnected eutectic lamellae (script-like features) in AC state to rods of low aspect ratio in the CE state, Fig. 4a.

Mechanical properties are slightly reduced by the exposure to 300 ? for both the as cast (AC) and extruded (CE) alloys, which is attributed to the variation of texture. The yield stress, tensile strength, and elongation at break for AC, AC-10, AC-100, CE, CE-10, and CE-100 states are shown in Table 3. The percent retention of the yield stress and tensile strength after annealing for 10 h is 76% and 85%, and after annealing for 100 h is 79%, and 88%.

Table 3 shows a comparison of the mechanical properties of binary Al-10Ce (from (Singh et al. 2024)) and ternary Al-10Ce-4Mg alloys in as cast, extruded and heat treated states. The corresponding stress-strain curves are compared in Fig. S3 of the SI. The extruded ternary alloy has much larger strength (390 MPa) compared to the binary alloy extruded in same conditions and to the same reduction (228 MPa), but it has lower strain at failure (17.2% compared with 22% in the binary CE case). The retention of yield stress and tensile strength in the case of the binary alloy is larger than 100% in both CE-10 and CE-100 states. The retention is significantly lower in the ternary case: 76% of the yield stress and 85% of the strength are retained after exposure to 300 °C for 10 h, and 79% and 88% of the yield stress and strength are retained after exposure to 300 °C for 100 h. The origin of this difference of behavior of the two types of alloys is explored further in Section High temperature mechanical properties.

Figure 7b shows microhardness test results. Each value represents a minimum of 10 measurements with the standard deviation indicated by the error bars. The hardness is 98, 105, 101, 114, 111, and 104 HV for AC, AC-10, AC-100, CE, CE-10, and CE-100, respectively. Generally, hardness and strength increase in proportion. This is not observed here when comparing the cast and extruded states. The cast samples showed some shrinkage porosity, which contributes to the reduced ductility and strength of cast samples relative to extruded samples, as seen in Fig. 7a. Porosity does not affect the hardness measurement. The hardness test results confirm the strong property retention upon exposure to elevated temperatures observed in the tensile tests and consistent with the microstructure-based observations discussed in the preceding section.

The fracture surfaces of Al-10Ce-4Mg samples were imaged to investigate the failure mechanisms and to correlate with microstructural features; images are shown in Fig. S4. Fracture surfaces of cast samples exhibit many cleavage facets, which indicate brittle failure. Fracture surfaces of extruded samples contain dimples, which indicates intense plastic deformation during failure. This agrees with the rather large strain at failure (17%) of the extruded samples.

High temperature mechanical properties

Al-10Ce-4Mg samples were further tested at 150 ?, 200 ? 250 ?, 300 ? and 350 ?. Samples were equilibrated at the test temperature and maintained at this temperature for the duration of the test. The stress-strain curves reported in Fig. 8 correspond to the CE material. The yield stress and the strength decrease with increasing temperature, as expected. Strain localization takes place at smaller strains as the temperature increases, while post-critical ductility increases.

For reference, we compare the temperature resistance of Al-10Ce-4Mg with that of AA2618, which is

Table 3 Comparison of mechanical properties of binary Al-10Ce, from (Singh et al. 2024), and ternary Al-10Ce-4Mg in the as cast and extruded states. The coefficient of variation of the yield stress and UTS for AC, AC-10 and AC-100 is between 2% and 5%, while that for the CE conditions is below 2%

	Binary Al-10Ce						Ternary Al-10Ce-4Mg					
	AC	AC-10	AC-100	CE	CE-10	CE-100	AC	AC-10	AC-100	CE	CE-10	CE-100
YS (MPa)	62	62	60	176	195	178	94	65	76	200	152	158
UTS (MPa)	127	131	136	228	251	227	132	102	108	390	332	344
%El	13.4	12.7	12.6	22.0	26.0	26.0	3.8	3.3	5.1	17.2	15.4	18.0

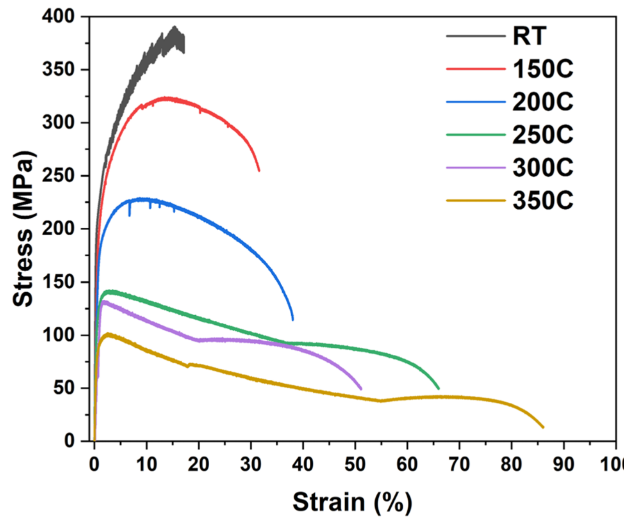

Fig. 8 Nominal stress-strain curves of Al-10Ce-4Mg in the CE state, at temperatures ranging from room temperature to 350 ?

considered a commercial high temperature Al alloys. Figure 9a shows the temperature dependence of the strength (UTS) of Al-10Ce (Singh et al. 2024) and Al-10Ce-4Mg, both in CE state and subjected to extrusion under same conditions and to the same reduction, compared with data for extruded pure Al (Kaufman 2018, Committee 1990) and AA2618 (T61 conditions) (Handbook 2019). Pure Al and AA2618 lose 80% and 90% of their room temperature strength, respectively, as the test temperature increases to 300 ?. The extruded Al-10Ce loses 34% of its room temperature strength under the same conditions, while Al-10Ce-4Mg loses 60%. However, the UTS reduction of the ternary takes place mostly below 250 °C, while above this temperature the UTS of the ternary is essentially identical to the UTS of the binary alloy. Hence, the room temperature UTS gain of Al-10Ce-4Mg relative to Al-10Ce is eliminated as the temperature increases to 250 °C.

Figure 9b shows the data in Fig. 9a normalized by the room temperature strength of the respective materials. The strength of pure Al decreases continuously as temperature increases (primarily in proportion to the reduction of the shear modulus). AA2618 exhibits three regimes: stage I, for $T < 150$? UTS decreases slower than in the pure Al case; stage II, for 150 ? $<$ $T < 250$?, UTS decreases fast due to the dissolution of the Al_2Cu q-phase and the increase of solubility of Cu in Al; stage III, for $T > 250$?, the softening rate becomes equal to that of pure Al. The binary Al-10Ce alloy exhibits an initial regime, for $T < 150$?, where UTS does not decrease with increasing temperature – a behavior reported in(Singh et al. 2024) for this particular alloy. For $T > 150$?, UTS decreases at the same rate with pure Al. Yet, the ternary Al-10Ce-4Mg alloy exhibits a behavior that combines features described for Al-10Ce and AA2618. Specifically,

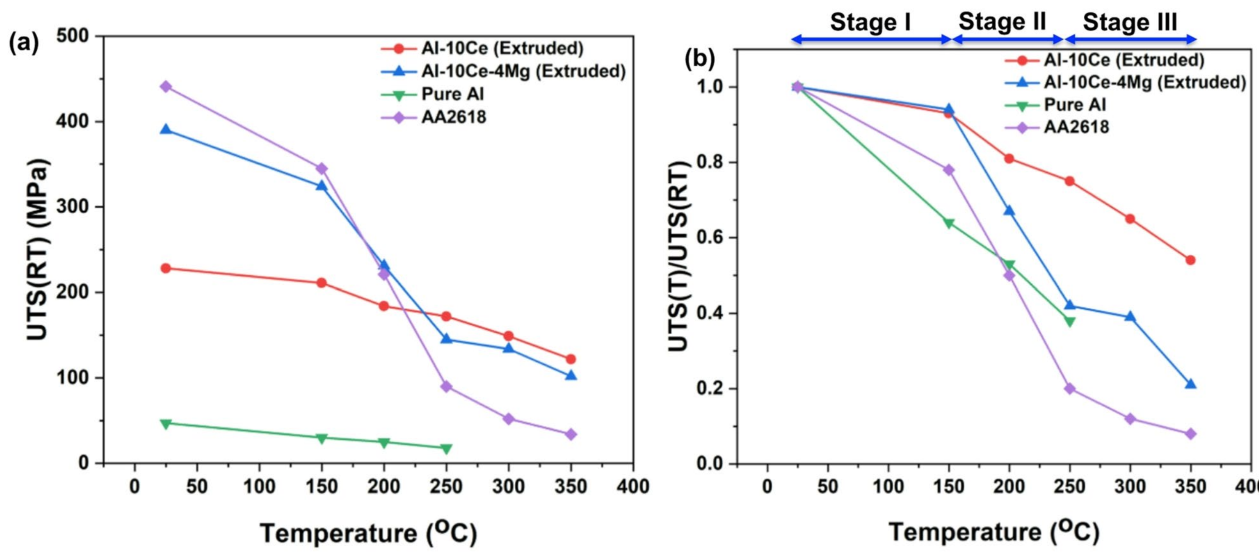

Fig. 9 (**a**) Dependence on temperature of the strength (UTS(T)) of Al-10Ce-4Mg in CE state compared with Al-10Ce extruded under same conditions and to the same reduction (Singh et al. 2024), with pure Al(Kaufman 2018, Committee 1990) and AA2618 (Handbook 2019). (**b**) Data in (**a**) normalized with the room temperature strength, UTS(RT), of the respective materials. Three stages are defined for the Al-10Ce-4Mg curve in (**b**)

UTS is independent of temperature for $T < 150$? (stage I), decreases rapidly in the temperature range 150 ? < $T < 250$? (stage II), after which the decay continues at the rate of Al-10Ce and pure Al (stage III).

These observations suggest that Al–Mg precipitates in Al-10Ce-4Mg are too fine to be identified by XRD and EBSD. For additional nanoscale characterization, TEM analysis was performed and representative results from a region away from any $Al_{11}Ce_3$ dispersoids are shown in Fig. 10. The HAADF (High-Angle Annular Dark-Field) image (Fig. 10a) reveals three Al–Mg matrix grains with slightly different orientation contrast. In addition, fine nanoscale precipitates are visible both along the grain boundaries/triple junction and within the grains, as marked by the white circles. These dark Z-contrast precipitates indicate the presence of lower-atomic-number elements. EDS mapping provides additional compositional information about the precipitates. However, the intragranular precipitates could not be clearly identified due to their small size, combined with effects from specimen thickness and the electron–beam interaction volume. In contrast, the EDS maps of the intergranular precipitates clearly show a high Mg concentration. Therefore, the TEM analysis provides evidence for the presence of Mg-rich precipitates. These precipitates are not visible in the XRD pattern, Fig. 1, likely due to their low volume fraction.

The UTS of CE Al-10Ce-4Mg decreases in the temperature range 150 ? < $T < 250$?, in which the Mg-rich precipitates dissolve, from 340 MPa to 150 MPa, drop that represents 48% of the room temperature UTS value, Fig. 9a. Pure Al softens by approximately 20% in the same temperature range. Hence, these precipitates contribute a large fraction of the room temperature strength. The DSC scan in Fig. 11 confirmed this precipitate dissolution event in Al-10Ce-4Mg sample. Figure 11b shows that there is an endothermic event for Al-10Ce-4Mg sample when it is heated. This endothermal event has an onset temperature of 215 ?. In contrast, there is no such event in the DSC curves for Al-10Ce, Fig. 11a, suggesting that there is no dissolution of precipitates for Al-10Ce up to at least 400 ?. A weak exothermic peak is seen on the cooling branch of the curve in Fig. 11b at ~360 ?, which, we consider, indicates formation of Mg-rich precipitates. This is supported by the observation that the stress-strain curves of the material before and after this heat treatment are identical, which indicates precipitation during cooling. We infer that Mg-rich precipitates account for about 55% of the room temperature flow stress. This issue is discussed further in Section Considerations related to the strengthening mechanisms.

Strain rate sensitivity of Al-10Ce-4Mg Alloy

The stress-strain curves shown in Fig. 8 are serrated, which is a manifestation of the Portevin-LeChatelier (PLC) effect caused by dynamic strain aging (DSA). The occurrence of this phenomenon is well documented in various solid solutions (Beukel 1975, Kubin and Estrin 1990, McCormick and Estrin 1989, Mulford and Kocks 1979), including Al-Mg alloys (Fujita and Tabata 1977, Balík and Lukáč 1993, Picu et al. 2005, Bintu et al. 2016).

Several mechanisms explaining DSA have been proposed (Fujita and Tabata 1977, Picu 2004), all being related to the diffusion of Mg atoms in the vicinity of dislocation cores. Being diffusion-controlled, the mechanisms are temperature dependent. Equivalently, PLC

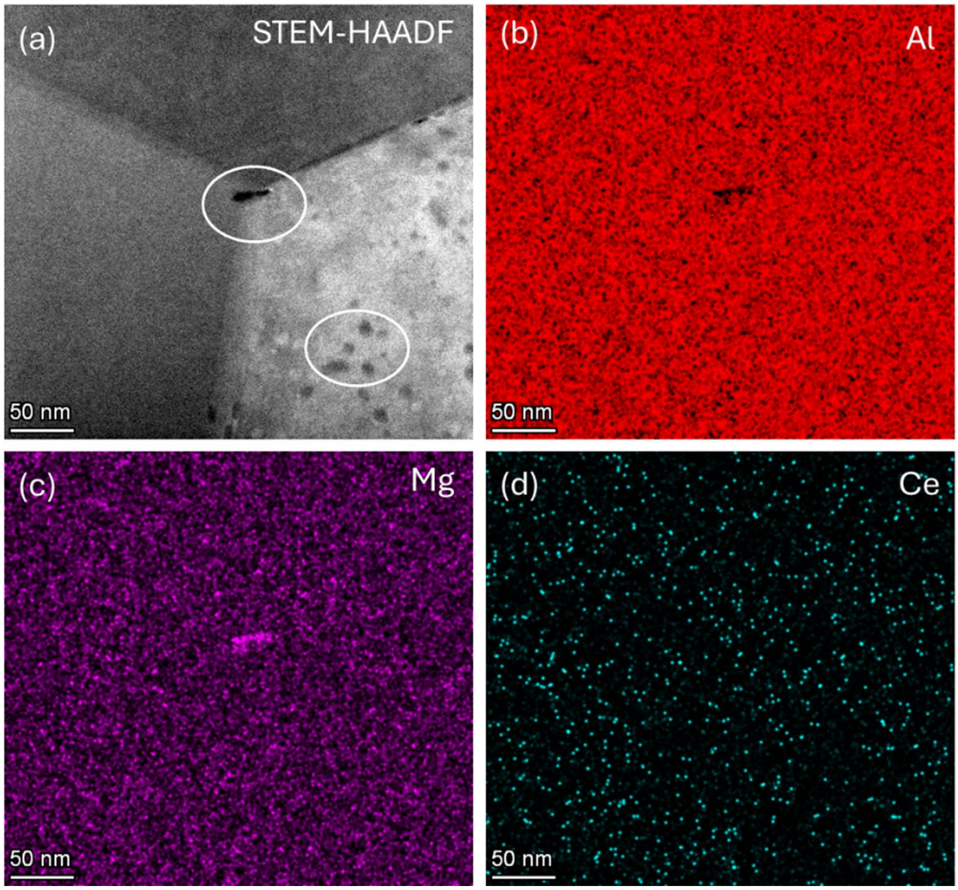

Fig. 10 STEM HAADF image and EDS map of Al-10Ce-4Mg alloy. (**a**) STEM-HAADF image of matrix (three grains forming a triple junction), (**b**-**d**) EDS map of (**b**) Al, (**c**) Mg, and (**d**) Ce. The white circles indicate the presence of Mg-rich precipitates

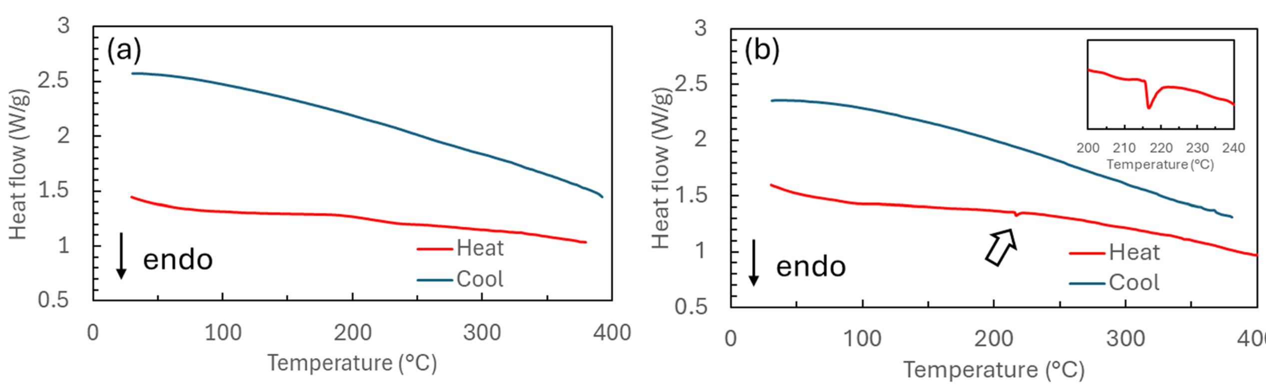

Fig. 11 DSC curves of (**a**) Al-10Ce and (**b**) Al-10Ce-4Mg samples. The inset shows a zoomed in region highlighting the endothermic peak

is both temperature and strain rate-dependent and it is common to observe the effect within specific ranges of temperatures and strain rates. To explore it, Al-10Ce-4Mg in the CE state was tested at various strain rates with $\dot{\epsilon}$ ranging from 10^{-2} to 10^{-5} s^{-1}, and the corresponding stress-strain curves are shown in Fig. 12. The curves are smooth (no PLC) for $\dot{\epsilon} = 10^{-2}\,s^{-1}$ and $\dot{\epsilon} = 10^{-5}\,s^{-1}$. Between these limits, the strain rate sensitivity is negative and strain-dependent. At $\dot{\epsilon} = 10^{-4}\,s^{-1}$, serrations begin beyond an incubation strain of 2%, with the strain rate sensitivity being zero (compare the curves for $\dot{\epsilon} = 10^{-5}\,s^{-1}$ and $\dot{\epsilon} = 10^{-4}\,s^{-1}$) for $\epsilon < 2\%$ and negative for $\epsilon > 2\%$. The incubation strain decreases as the strain rate increases to $\dot{\epsilon} = 10^{-3}\,s^{-1}$. The strain rate range in which negative rate sensitivity is observed at room temperature is similar to that reported for the commercial alloy AA5182 which has 4.5% Mg (Picu et al. 2005). The effect of temperature on PLC is

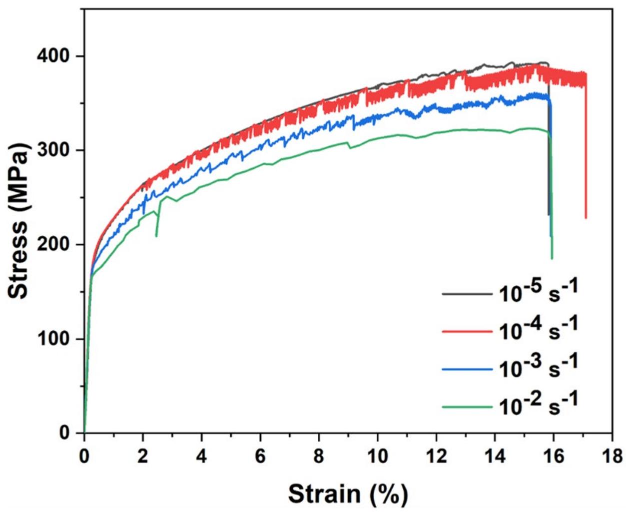

Fig. 12 Effect of strain rates on engineering stress-strain curves of Al-10Ce-4Mg in CE state tested at room temperature

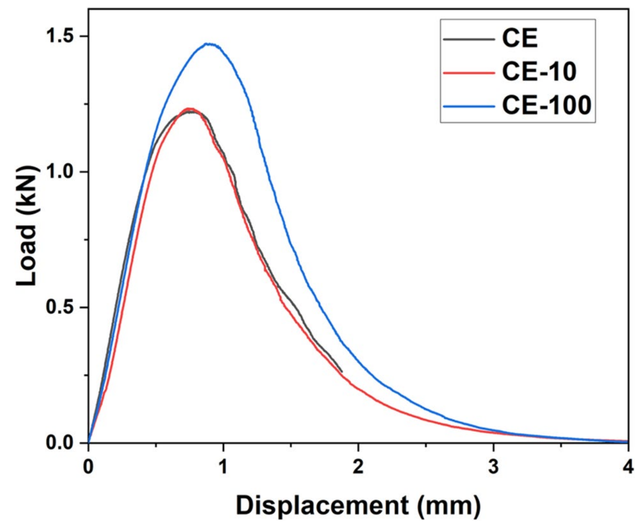

Fig. 13 Load-displacement curves of notched CE, CE-10 and CE-100 samples loaded in the 3-point bend configuration

visible in Fig. 8, where the room temperature stress-strain curve is serrated (PLC), while the curve at 150 ? is smooth (no PLC). The strain rate sensitivity parameter, $m = \partial \log\sigma / \partial \log\dot{\epsilon}$, was calculated based on the curves in Fig. 8 for strains larger than 5%. At $\dot{\epsilon} = 10^{-4}\, s^{-1}$ and $\dot{\epsilon} = 10^{-3}\, s^{-1}$, m = – 0.03. m increases towards the positive range as the strain rate increases or decreases away from the range shown in Fig. 8. These observations indicate that sufficient Mg remains in solid solution to produce negative rate sensitivity and a macroscopically-observable PLC effect.

Fracture toughness of cast and extruded Al-10Ce-4Mg alloys

The fracture toughness was measured using the single-edge bend configuration with load-line displacement method (ASTM-E1820 2009) for the alloy in CE, CE-10 and CE-100 states (ASTM). This requires determining the area under the force-displacement curve obtained in a 3-point bend test using a notched (including pre-crack) sample up to the maximum force value. Equations (2) and (3) provide the elastic and plastic components of the energy release rate (ASTM):

$$J_{el} = \frac{K_Q^2(1-\nu^2)}{E}, \tag{2}$$

$$J_{pl} = \frac{\eta_{pl} A_{pl}}{B(W-a_0)}, \tag{3}$$

where ν and E are the Poisson's ratio and elastic modulus, and K_Q is the stress intensity factor at fracture. ν and E are taken to be 0.34 and 70 GPa, as per our test results. η_{pl} is taken to be 1.9 per the ASTM E-1820 standard. A_{pl} is the area under the load-displacement curve calculated up to the maximum point. Parameters S, W, B, and a_o are the loading span length, specimen width and thickness, and the notch length, respectively. The critical energy release rate, J_{Ic}, is the sum of Eqs. (2) and (3):

$$J = J_{el} + J_{pl} \tag{4}$$

The load vs. displacement of CE, CE-10, and CE-100 are shown in Fig. 13. The ternary extruded and heat-treated samples have toughness values of 20.3 $\pm$ 0.85 kJ/m^2, 15.5 $\pm$ 0.80 kJ/m^2, and 24.3 $\pm$ 1.21 kJ/m^2 for CE. CE-10, and CE-100, respectively. Component J_{pl} (18 kJ/m^2, 13 kJ/m^2, 21 kJ/m^2) is larger than J_{el} (2.3 kJ/m^2, 2.5 kJ/m^2, 3.3 kJ/m^2) since these materials are ductile. These values are obtained by performing 3 repeats for each case. The annealed and non-annealed samples show similar fracture toughness which, again, demonstrates the thermal stability of this alloy. These values are comparable with some of the largest fracture toughness values reported for Al alloys, such as for wire-arc DED-processed Al-Si (J_c =36.8 kJ/m^2) (Paul et al. 2022), Al-Li ($J_c \approx$ 26 kJ/m^2(Lynch et al. 2014) and Al2618 ($J_c =$ 10.34 kJ/m^2) (Gariboldi et al. 2007).

Considerations related to the strengthening mechanisms

Solid solution and grain size strengthening, strain hardening and precipitation strengthening (due to $Al_{11}Ce_3$ and nanoscale Mg-rich precipitates) are expected to be active strengthening mechanisms in this alloy. Solid solution strengthening is associated with the Mg solute in Al, while Ce has too low solubility in Al to increase the flow stress through this mechanism.

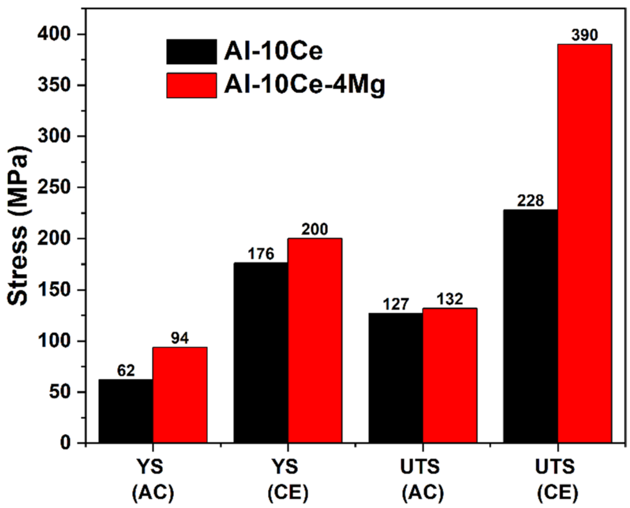

Fig. 14 Yield stress and UTS of Al-10Ce (data from (Singh et al. 2024)) and Al-10Ce-4Mg in as cast (AC) and extruded (CE) states. Values of these stresses (in MPa) are shown above the bars

Figure 14 shows the yield stress and UTS of as cast and extruded states of binary Al-10Ce (Singh et al. 2024) and ternary Al-10Ce-4Mg alloys, with the binary alloy being extruded in the same conditions as used here for the ternary. Comparing these stress values provides insight into the contribution to the flow stress of the various mechanisms. Specifically, the effect of microstructural refinement due to extrusion (both grain and dispersoid refinement) emerges by comparing the yield stress of Al-10Ce AC and CE states; this mechanism contributes 114 MPa to the yield stress. Same processing conditions applied to Al-10Ce-4Mg lead to similar refinement and an increase of the yield stress of 106 MPa, consistent with the value for the equivalent binary alloy. This increase is also due, in part, to the increase of the dislocation density by a factor of 2 between cast and extruded states, Table 3, which is expected to produce an increase of the yield stress of $\sqrt{2}$ (or ~41%, i.e. 52 MPa) relative to the AC state. Hence, we conclude that the increase of 106 MPa in yield stress of Al-10Ce-4Mg is due in equal proportions to the increase of the dislocation density and to grain and intermetallic refinement.

Comparing the yield stress of Al-10Ce and Al-10Ce-4Mg both in the AC state, indicates that the addition of Mg contributes only 32 MPa to the yield stress.

Comparing the yield stress with UTS sheds light on the strain hardening ability of the material. The ability of the binary alloy to strain harden is limited (difference between UTS and yield stress of 65 MPa and 52 MPa in the AC and CE states). However, the ternary alloy in the CE state strain hardens by 190 MPa. This much larger strain hardening effect, compared to the binary alloy, can be attributed to the influence of a fine dispersion of Mg-rich nanoscale precipitates, which correlates with the TEM observations shown in Fig. 10.

Conclusion

The effect of extrusion on the microstructure and mechanical properties of Al-10Ce-4Mg is evaluated in this work in conjunction with the material's ability to retain properties upon exposure to elevated temperatures. The as-cast alloy has large grain size and relatively low yield stress and strength, while the effect of Mg in Al-Ce is not profound in the cast state. Significant microstructural refinement is observed upon extrusion which leads to both grain size reduction and a decrease of the size of $Al_{11}Ce_3$ intermetallics. Extrusion increases the yield stress, ultimate tensile strength, and elongation at failure by factors of 2.5, 2.5, and 4.5, respectively. These properties are largely preserved after annealing at 300 °C for up to 100 h. The toughness is also preserved upon annealing at 300 °C for up to 100 h. The strength at elevated temperatures decreases relative to the room temperature strength, with a rapid decrease in the 150 ? to 250 ? range. This is attributed to the dissolution of nanoscale Mg-rich precipitates which have been identified by TEM in the extruded alloy. The ratio of the UTS at 300 ? to the room temperature UTS is 0.39, lower than that of the equivalent binary alloy, Al-10Ce (ratio 0.65), but larger than the high temperature commercial alloy AA2618 (ratio 0.1). The study shows that adequate thermomechanical processing and associated microstructural refinement render these alloys potentially useful in applications requiring resistance to elevated temperatures.

Supplementary Information

The online version contains supplementary material available at https://doi.org/10.1007/s44492-026-00011-3.

Supplementary Material 1 (DOCX 5.73 MB)

Acknowledgements

This work was supported by the US Department of Energy (DOE) through Grant No. DE-EE0010219.

Author contributions

G.S., H.O and H.T: investigation, methodology, data curation. G.S. wrote the first draft of the manuscript. M-C.K. and L.Z.: investigation. G.O., M.S., C.J., R.N. and C.P.: conceptualization, methodology, funding, supervision. All authors reviewed the manuscript.

Funding

This work was supported by the US Department of Energy (DOE) through Grant No. DE-EE0010219.

Data availability

The data resulting from this investigation is included in the article.

Declarations

Ethics, consent to participate, and consent to publish declarations

Not applicable

Competing interests

The authors declare no competing interests.

Financial interests

The authors have no relevant financial or non-financial interests to disclose.

Received: 20 April 2026 / Accepted: 18 May 2026
Published online: 01 June 2026

References

Gao YH, Yang C, Zhang JY, Cao LF, Liu G, Sun J, Ma E (2019) Stabilizing nanoprecipitates in Al-Cu alloys for creep resistance at 300°C. Mater Res Lett 7:18–25. https://doi.org/10.1080/21663831.2018.1546773

Mondol S, Alam T, Banerjee R, Kumar S, Chattopadhyay K (2017) Development of a high temperature high strength Al alloy by addition of small amounts of Sc and Mg to 2219 alloy. Mat Sci Eng A 687:221–231. https://doi.org/10.1016/J.MSEA.2017.01.037

Guo Y, Hu J, Han Q, Sun B, Wang J, Liu C (2022) Microstructure diversity dominated by the interplay between primary intermetallics and eutectics for Al-Ce heat-resistant alloys. J Alloys Compd 899:162914. https://doi.org/10.1016/j.jallcom.2021.162914

Shen S, Wu C, Li Y, Huang Y, Huang W, Zhang P, Zhong S, Lu Y, Luo G, Gan Z, Liu J (2023) Refining mechanism and elevated-temperature mechanical properties of Al-Ce alloys solidified under super gravity field. Mat Sci Eng A 879:145191. https://doi.org/10.1016/j.msea.2023.145191

Nam S, Simsek E, Argibay N, Rios O, Henderson HB, Weiss D, Moore EE, Perron AP, McCall SK, Ott RT (2023) Strength mechanisms and tunability in Al-Ce-Mg ternary alloys enabled by additive manufacturing. Mater Des 231:112009. https://doi.org/10.1016/j.matdes.2023.112009

Singh G, Odhiambo HW, Bin Tasneem MH, Ouyang G, Soare MA, Cui J, Napolitano RE, Picu CR (2024) Effect of thermomechanical processing on mechanical properties and the microstructure of binary Al-Ce alloy. Mater Sci Engineering: A 916:147395. https://doi.org/10.1016/j.msea.2024.147395

Stojanovic B, Bukvic M, Epler I (2018) Application of Aluminum and Alluminum alloys in engineering. Appl Eng Lett 3:2466–4847. https://doi.org/10.18485/aeletters.2018.3.2.2

Sims ZC, Weiss D, McCall SK, McGuire MA, Ott RT, Geer T, Rios O, Turchi PAE (2016) Cerium-Based, Intermetallic-Strengthened Aluminum Casting Alloy: High-Volume Co-product Development. J Matls 68:1940–1947. https://doi.org/10.1007/s11837-016-1943-9

El-Hadad S, Moussa ME, Riedel E, Ahmed M, Bähr R, Nofal A (2023) Solidification Processing of Al-Ce Alloys for High-Temperature Applications, in: INALCO 2023, MDPI, Basel Switzerland, : p. 17. https://doi.org/10.3390/engproc2023043017

Weiss D, Cerium IH-TAAC (2019) J Mater Eng Perform 28:1903–1908. https://doi.org/10.1007/s11665-019-3884-2

Huda Z, Edi P (2013) Materials selection in design of structures and engines of supersonic aircrafts: A review. Mater Design 46:552–560. https://doi.org/10.1016/J.MATDES.2012.10.001

Sims ZC, Kesler MS, Henderson HB, Castillo E, Fishman T, Weiss D, Singleton P, Eggert R, McCall SK, Rios O (2022) How Cerium and Lanthanum as Coproducts Promote Stable Rare Earth Production and New Alloys. J Sust Metall 8:1225–1234. https://doi.org/10.1007/s40831-022-00562-4

Czerwinski F (2019) Cerium in aluminum alloys. J Mat Sci 55:24–72. https://doi.org/10.1007/S10853-019-03892-Z

Sims ZC, Rios OR, Weiss D, Turchi PEA, Perron A, Lee JRI, Li TT, Hammons JA, Bagge-Hansen M, Willey TM, An K, Chen Y, King AH, McCall SK (2017) High performance aluminum-cerium alloys for high-temperature applications. Mater Horiz 4:1070–1078. https://doi.org/10.1039/c7mh00391a

Perrin AE, Michi RA, Leonard DN, Sisco KD, Plotkowski AJ, Shyam A, Poplawsky JD, Allard LF, Yang Y (2023) Effect of Mn on eutectic phase equilibria in Al-rich Al-Ce-Ni alloys. J Alloys Compd 965:171455. https://doi.org/10.1016/j.jallcom.2023.171455

Okamoto H (2011) Al-Ce (Aluminum-Cerium). J Phase Equilib Diffus 32:392–393. https://doi.org/10.1007/S11669-011-9914-X/TABLES/1

Cao Z, Kong G, Che C, Wang Y, Peng H (2017) Experimental investigation of eutectic point in Al-rich Al-La, Al-Ce, Al-Pr and Al-Nd systems. J Rare Earths 35:1022–1028. https://doi.org/10.1016/S1002-0721(17)61008-1

Dai K, Ye J, Wang Z, Chen J, He C, Xiong K (2023) Beneficial Utilization of Electromagnetic Stirring Technology in Al-Ce Alloys. J Matls 75:2788–2798. https://doi.org/10.1007/s11837-023-05904-5

Sun Y, Hung C, Hebert RJ, Fennessy C, Tulyani S, Aindow M (2019) Eutectic microstructures in dilute Al-Ce and Al-Co alloys. Mater Charact 154:269–276. https://doi.org/10.1016/j.matchar.2019.06.010

Kozakevich JR, Stroh J, Sediako D, Weiss D (2023) Solidification Kinetics of an Al-Ce Alloy with Additions of Ni and Mn, Metals (Basel). 13:955. https://doi.org/10.3390/met13050955

Ye J, Dai K, Gao M, Chen J, Guan R (2023) Primary phase transformation mechanism in a hypereutectic Al-Ce alloy during rapid solidification. Mater Lett 340:134172. https://doi.org/10.1016/j.matlet.2023.134172

Rogachev SO, Naumova EA (2021) Thermal Stability of Al-Ca and Al-Ce Alloys Obtained by High-Pressure Torsion. J Mater Eng Perform 30:9192–9199. https://doi.org/10.1007/s11665-021-06105-4

Plotkowski A, Sisco K, Bahl S, Shyam A, Yang Y, Allard L, Nandwana P, Rossy AM, Dehoff RR (2020) Microstructure and properties of a high temperature Al–Ce–Mn alloy produced by additive manufacturing. Acta Mater 196:595–608. https://doi.org/10.1016/j.actamat.2020.07.014

Rogachev SO, Naumova EA, Lukina EA, Zavodov AV, Khatkevich VM (2021) High strength al–la, al–ce, and al–ni eutectic aluminum alloys obtained by high-pressure torsion. Materials 14:6404. https://doi.org/10.3390/ma14216404

Sisco K, Plotkowski A, Yang Y, Leonard D, Stump B, Nandwana P, Dehoff RR, Babu SS (2021) Microstructure and properties of additively manufactured Al–Ce–Mg alloys. Sci Rep 11:6953. https://doi.org/10.1038/s41598-021-86370-4

D'Souza AD, Rao SS, Herbert MA (2019) Assessment of influence of process parameters on properties of friction stir welded Al-Ce-Si-Mg aluminium alloy. Mater Res Express 6:086504. https://doi.org/10.1088/2053-1591/ab1aec

Zhang C, Wang Y, Lv H, Gao H, Wang J, Sun B (2021) Enhanced load transfer and ductility in Al–9Ce alloy through heterogeneous lamellar microstructure design by cold rolling and annealing. Mat Sci Eng A 821:141591. https://doi.org/10.1016/j.msea.2021.141591

Czerwinski F, Shalchi Amirkhiz B, Aluminum Cast Alloys Based on the Al–Ce–Si–Mg System: An Influence of Silicon on Crystallization, Phase Composition, and, Properties T (2022) Metall. Mater. Trans. A 53 4233–4246. https://doi.org/10.1007/s11661-022-06812-0

Gröbner J, Kevorkov D, Schmid-Fetzer R (2002) Thermodynamic modeling of Al–Ce–Mg phase equilibria coupled with key experiments. Intermetallics 10:415–422. https://doi.org/10.1016/S0966-9795(02)00018-3

Lv H, Peng P, Feng T, Gao H, Ju J, Wang B, Wang J, Sun B (2022) High-performance co-continuous Al-Ce-Mg alloy with in-situ nano-network structure fabricated by laser powder bed fusion. Addit Manuf 60:103218. https://doi.org/10.1016/j.addma.2022.103218

Hu B, Quan B, Li D, Wang X, Li Z, Zeng X (2021) Solid solution strengthening mechanism in high pressure die casting Al–Ce–Mg alloys. Mater Sci Engineering: A 812:141109. https://doi.org/10.1016/j.msea.2021.141109

Wang Y, Liang X, Zeng L, Wu H, Li H (2022) The microstructure evolution of Al-5Ce alloy prepared by strain-induced melt activation during semi-solid isothermal treatment process. Mater Lett 326. https://doi.org/10.1016/j.matlet.2022.132948

Wang W, Pan Q, Lin G, Wang X, Sun Y, Wang X, Ye J, Sun Y, Yu Y, Jiang F, Li J, Liu Y (2020) Al-Ce-Zr and Al-Ce-Sc-Y alloy conductors processed by die casting, hot extrusion and cold drawing. J Mater Sci Technol 58:155–170. https://doi.org/10.1016/j.jmst.2020.03.073. Microstructure and properties of novel Al-Ce-Sc, Al-Ce-Y

Milligan B, Reza-E-Rabby M, Schuessler B, Roosendaal T, Lemmon T, Whalen S (2024) Microstructural refinement of an Al-Ce-Mg alloy via Shear Assisted Processing and Extrusion. Mater Sci Engineering: A 916:147328. https://doi.org/10.1016/j.msea.2024.147328

Odhiambo HW, Singh G, Tasneem M, Soare MA, Leszczewicz J, Cui J, Napolitano RE, Ouyang G, Picu CR (2025) Al–Ce-Based Alloys: Processing, Mechanical Properties, and High-Temperature Stability, in Light Metals 2025, Ed. L. Edwards, : pp. 87–96. https://doi.org/10.1007/978-3-031-80676-6_10

Moore EE, Turchi PEA, Lordi V, Weiss D, Sims ZC, Henderson HB, Kesler MS, Rios O, McCall SK, Perron A (2020) Thermodynamic Modeling of the Al-Ce-Cu-Mg-Si System and Its Application to Aluminum-Cerium Alloy Design. J Phase Equilib Diffus 41:764–783. https://doi.org/10.1007/s11669-020-00852-y

E8/E8M (2013) Standard Test Methods for Tension Testing of Metallic Materials, ASTM International

E384-17 A (2016) Standard Test Method for Microindentation Hardness of Materials. https://doi.org/10.1520/E0384-17

ASTM Standard E1820-11 (2009) Standard Test Method for Measurement of Fracture Toughness

Jones H (2005) Some effects of solidification kinetics on microstructure formation in aluminium-base alloys. Mater Sci Engineering: A 413–414. https://doi.org/10.1016/j.msea.2005.08.190

Basu I, Ocelík V, De Hosson JTM (2018) BCC-FCC interfacial effects on plasticity and strengthening mechanisms in high entropy alloys. Acta Mater 157:83–95. https://doi.org/10.1016/J.ACTAMAT.2018.07.031

Kamaya M (2012) Assessment of local deformation using EBSD: Quantification of local damage at grain boundaries. Mater Charact 66:56–67. https://doi.org/10.1016/j.matchar.2012.02.001
Sun SJ, Tian YZ, Lin HR, Wang ZJ, Zhang ZF (2021) Revisiting the role of prestrain history in the mechanical properties of ultrafine-grained CoCrFeMnNi high-entropy alloy. Mater Sci Engineering: A 801:140398. https://doi.org/10.1016/j.msea.2020.140398
Kaufman JG (2018) Properties of Pure Aluminum. Alum Sci Technol 31–43. https://doi.org/10.31399/ASM.HB.V02A.A0006505
Committee AH (1990) Properties and Selection: Nonferrous Alloys and Special-Purpose Materials, Properties and Selection: Nonferrous Alloys and Special-Purpose Materials https://doi.org/10.31399/ASM.HB.V02.9781627081627
Handbook ASM, Anderson K, Weritz J, Kaufman JG (eds) (2019) 2618 and 2618A: Al-Cu-Mg-Ni Alloys for High-Temperature Service, Properties and Selection of Aluminum Alloys 328–32. https://doi.org/10.31399/ASM.HB.V02B.A0006616
van den Beukel A (1975) Theory of the effect of dynamic strain aging on mechanical properties. Phys Stat Sol (a) 30:197–206. https://doi.org/10.1002/pssa.2210300120
Kubin LP, Estrin Y (1990) Evolution of dislocation densities and the critical conditions for the Portevin-Le Châtelier effect. Acta Metall Mater 38:697–708. https://doi.org/10.1016/0956-7151(90)90021-8
McCormick PG, Estrin Y (1989) Transient flow behaviour associated with dynamic strain ageing. Scripta Metall 23:1231–1234. https://doi.org/10.1016/0036-9748(89)90332-3
Mulford RA, Kocks UF (1979) New observations on the mechanisms of dynamic strain aging and of jerky flow. Acta Metall 27:1125–1134. https://doi.org/10.1016/0001-6160(79)90130-5
Fujita H, Tabata T (1977) Discontinuous deformation in Al-Mg alloys under various conditions. Acta Metall 25:793–800. https://doi.org/10.1016/0001-6160(77)90094-3
Balík J, Lukáč P (1993) Portevin-Le chatelier instabilities in Al-3 Mg conditioned by strain rate and strain. Acta Metall Mater 41:1447–1454. https://doi.org/10.1016/0956-7151(93)90253-O
Picu RC, Vincze G, Ozturk F, Gracio JJ, Barlat F, Maniatty AM (2005) Strain rate sensitivity of the commercial aluminum alloy AA5182-O. Mat Sci Eng A 390:334–343. https://doi.org/10.1016/j.msea.2004.08.029
Bintu A, Vincze G, Picu RC, Lopes AB (2016) Effect of symmetric and asymmetric rolling on the mechanical properties of AA5182. Mater Des 100:151–156. https://doi.org/10.1016/j.matdes.2016.03.123
Picu RC (2004) A mechanism for the negative strain-rate sensitivity of dilute solid solutions. Acta Mater 52:3447–3458. https://doi.org/10.1016/j.actamat.2004.03.042
Paul MJ, Klein T, Simson C, Niedermayer J, Kruzic JJ, Gludovatz B (2022) Strength and fracture resistance of in-situ alloyed compositionally-graded Al-Si processed by dual-wire arc directed energy deposition. Addit Manuf 60:103291. https://doi.org/10.1016/j.addma.2022.103291
Lynch SP, Wanhill RJH, Byrnes RT, Bray GH (2014) Fracture Toughness and Fracture Modes of Aerospace Aluminum–Lithium Alloys. Aluminum-Lithium Alloys. Elsevier, pp 415–455. https://doi.org/10.1016/B978-0-12-401698-9.00013-6.
Gariboldi E, Ripamonti D, Signorelli L, Vimercati G, Casaro F (2007) Fracture toughness and microstructure in AA 2XXX aluminum alloys. Metall Sci Tecnol 25:3–11

Publisher's note